International Forum on Aeroelasticity and Structural Dynamics
IFASD 2017
25-28 June 2017 Como, Italy

LIMIT CYCLE OSCILLATIONS OF CANTILEVER RECTANGULAR FLAT PLATES IN A WIND TUNNEL

N. Giannelis[1], G. A. Vio[1], G. Dimitriadis[2]

[1]Aerospace, Mechanical and Mechatronic Engineering Department
University of Sydney, New South Wales, Australia

[2]Aerospace and Mechanical Engineering Department
University of Liège, 4000 Liège, Belgium

Keywords: Flutter, Limit Cycle Oscillations, Von Kármán thin plate theory, Vortex Lattice method

Abstract: A closed form state-space model of the nonlinear aeroelastic response of thin cantilevered flat plates is derived using a combination of Von Kármán thin plate theory and a linearized continuous time vortex lattice aerodynamic model. The modal-based model is solved for the amplitude and period of the limit cycles of the flat plates using numerical continuation. The resulting predictions are compared to experimental data obtained from identical flat plates in the wind tunnel. It is shown that the aeroelastic model predicts the linear flutter conditions and nonlinear response of the plates with reasonable accuracy, although the predicted limit cycle amplitude variation with airspeed is different to the one measured experimentally due to unmodelled physics.

1 INTRODUCTION

The aim of this work is to investigate experimentally and numerically the limit cycle oscillations of cantilever flat plates in low speed airflows and at different angles of attack. In particular, the applicability of Von Kármán thin plate theory to the structural modelling of this problem will be assessed. Weiliang and Dowell [1] applied this theory to a cantilever rectangular plate oscillating in supersonic flow. Subsequent applications concerned low speed flows around both rectangular [2] and triangular [3] plates (Delta wings). [4] found that Von Kármán plate theory predictions do not match either experimental data or responses obtained from a higher fidelity structural model. [5] studied the convergence behaviour of Rayleigh-Ritz series solutions of the Von Kármán plate equations, finding that using in-plane mode shapes identical to those calculated from a finite element model for the out-of-plane displacements yielded the fastest convergence.

Attar et al [6] showed that the effect of steady angle of attack on flutter speed is very small for low-speed Delta wings. In contrast, simulations based on Von Kármán plate theory showed that the flutter speed can decrease [7], increase [6] or remain relatively constant [6] with steady angle of attack. Furthermore, Korbahti et al [8] presented experimental results showing that the instability onset airspeed of a Delta wing at low speeds decreases with steady angle of attack. Another objective of the present work is to investigate the behaviour of the flutter speed of cantilever plates of different aspect ratios and sweeps as the steady angle of attack is varied.

2 EXPERIMENTS

The experiments were carried out in the 3 ft by 4 ft low-speed wind tunnel of the University of Sydney, whose top speed is 60 m/s. Six aluminium cantilever plates were tested; they all had a constant chord length, c, of 20 cm and thickness 1 mm. The AR2.25 plate had a span, s, of 45 cm, the span of the AR3 plate was 60 cm while the span of all four AR4 plates was 80 cm. The AR4 plates featured four different values of sweep angle, Λ, 0°, 10°, 20°, 45°. All plates were clamped to the wooden floor of the wind tunnel using a pair of aluminium brackets and steel bolts. Two values of the steady angle of attack were considered, $\alpha_0 = 0^\circ$ and 5°. Figure 1 shows photographs of two of the AR4 wings installed in the wind tunnel.

(a) 0° sweep (b) 20° sweep

Figure 1: Two AR4 wings installed in the wind tunnel

The instrumentation consisted of a single high speed SONY RX-100 IV camera, filming at 250 frames per second. The resulting videos were analysed using the Tracker software by Open Source Physics. Targets were drawn on each wing and their positions on each frame were extracted by the software. The fact that only one camera was used meant that the resulting displacement data is a 2D projection of the 3D motion of the wings. Nevertheless, as the position of the camera with respect to the wing and the focal length were recorded, these projections can be used for quantitative comparisons between experimental measurements and simulation predictions.

All the plates started undergoing Limit Cycle Oscillations (LCOs) at a specific critical airspeed, which differed for each Λ and AR value. For example, figure 2(a) shows the variation of the limit cycle amplitude with airspeed observed for the $\Lambda = 20^\circ$ wing. The plotted data is horizontal and vertical displacement of the wingtip of the trailing edge on the movie frames. The amplitude grows with airspeed, therefore it is concluded that the bifurcation is supercritical and, hence, the bifurcation airspeed is the flutter speed of the underlying linear system. Figure 2(b) plots the frequency content of the time response of the wing tip of the trailing edge at all airspeeds where LCOs were observed. It shows that the fundamental frequency of oscillation for this plate is around 6 Hz and varies very slowly with airspeed. The LCO frequency at the flutter airspeed is taken as the flutter frequency.

	AR=2.25 $\Lambda = 0^\circ$	AR=3 $\Lambda = 0^\circ$	AR=4 $\Lambda = 0^\circ$	AR=4 $\Lambda = 10^\circ$	AR=4 $\Lambda = 20^\circ$	AR=4 $\Lambda = 45^\circ$
Q_f	30.0 m/s	21.2	17.1 m/s	16.8 m/s	15.8 m/s	13.4 m/s
k_f	15.0 Hz	9.5 Hz	8.0 Hz	6.3 Hz	5.8 Hz	4.2 Hz

Table 1: Experimentally measured flutter speed and frequency for all wings

Table 1 presents the flutter speed and frequency measurements for each of the wings and shows

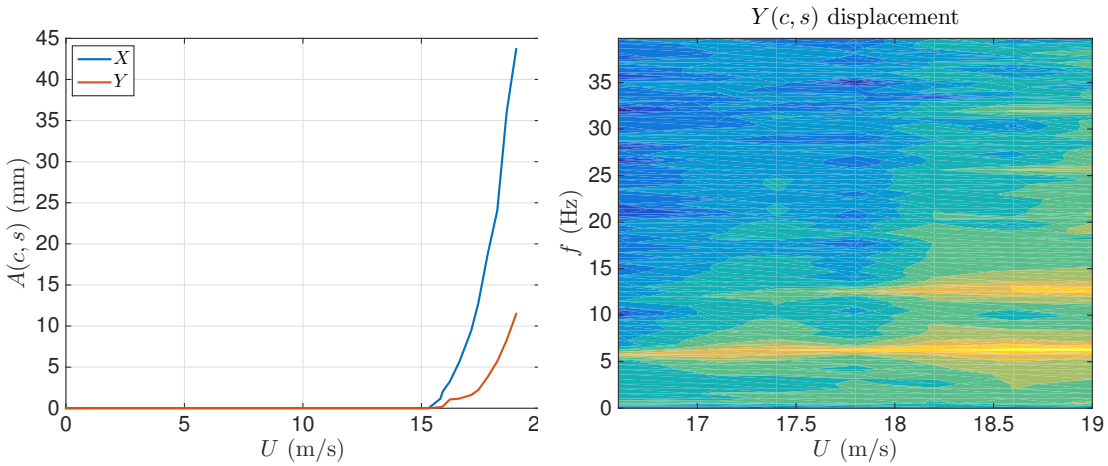

(a) Amplitude (b) Frequency

Figure 2: Limit cycle amplitude and frequency variation with airspeed for the wing with AR=4, $\Lambda = 20°$

that they both decrease with increasing sweep angle and aspect ratio. As the span of the plates is constant, increasing the sweep and/or the aspect ratio means that the wings become more flexible, i.e. their natural frequencies decrease.

3 MATHEMATICAL MODEL

The mathematical model used in this work consists of a combination of Von Kármán's thin plate theory and the Vortex Lattice aerodynamic modelling method, as described by Dimitradis [9]. Weiliang and Dowell [1] applied a Rayleigh-Ritz methodology to derive the equations of motion. The displacements u, v and w are written as series of the form

$$\begin{aligned} u(x,y,t) &= \sum_{j=1}^{m_p} u_j(x,y)p_j(t) \\ v(x,y,t) &= \sum_{j=1}^{m_q} v_j(x,y)q_j(t) \\ w(x,y,t) &= \sum_{j=1}^{m_r} w_j(x,y)r_j(t) \end{aligned} \tag{1}$$

where $u_j(x,y)$, $v_j(x,y)$, $w_j(x,y)$ are mode shapes and $p_j(t)$, $q_j(t)$, $r_j(t)$ are generalised coordinates. The numbers m_p, m_q and m_r of modes u_j, v_j and w_j respectively can be distinct but usually $m_p = m_q$. The out-of-plane kinetic energy of the flat plate is then given by

$$T = \frac{m_m}{2}\int_0^s \int_0^c \dot{w}^2 \mathrm{d}x\mathrm{d}y \tag{2}$$

where $m_m = \rho_m h$ is the mass per unit area. The kinetic energies in the x and y directions are assumed to be negligible. The elastic energy is obtained from Von Kármán's thin plate theory applied to a plate of finite span, as detailed in Weiliang and Dowell [1]. The total elastic energy of the plate is given by

$$U = U_s + U_b \tag{3}$$

where U_s is the stretching energy

$$\begin{aligned} U_s &= \frac{Eh}{2(1-\nu^2)} \int_0^s \int_0^c \left\{ \left(\frac{\partial u}{\partial x} + \frac{1}{2} \left(\frac{\partial w}{\partial x} \right)^2 \right)^2 + \left(\frac{\partial v}{\partial y} + \frac{1}{2} \left(\frac{\partial w}{\partial y} \right)^2 \right)^2 \right. \\ &+ 2\nu \left(\frac{\partial u}{\partial x} + \frac{1}{2} \left(\frac{\partial w}{\partial x} \right)^2 \right) \left(\frac{\partial v}{\partial y} + \frac{1}{2} \left(\frac{\partial w}{\partial y} \right)^2 \right) \\ &\left. + \frac{1-\nu}{2} \left(\frac{\partial v}{\partial x} + \frac{\partial u}{\partial y} + \frac{\partial w}{\partial x} \frac{\partial w}{\partial y} \right)^2 \right\} \mathrm{d}x\mathrm{d}y \end{aligned} \tag{4}$$

and U_b is the bending energy

$$U_B = \frac{D}{2} \int_0^s \int_0^c \left\{ \left(\frac{\partial^2 w}{\partial x^2} \right)^2 + \left(\frac{\partial^2 w}{\partial y^2} \right)^2 + 2\nu \frac{\partial^2 w}{\partial x^2} \frac{\partial^2 w}{\partial y^2} + 2(1-\nu) \left(\frac{\partial^2 w}{\partial x \partial y} \right)^2 \right\} \mathrm{d}x\mathrm{d}y \tag{5}$$

The equations of motion for the problem can be derived using Lagrance's equations

$$\begin{aligned} \frac{\partial L}{\partial p_i} &= 0 \\ \frac{\partial L}{\partial q_i} &= 0 \\ \frac{\mathrm{d}}{\mathrm{d}t} \left(\frac{\partial L}{\partial \dot{r}_i} \right) - \frac{\partial L}{\partial r_i} &= Q_i \end{aligned} \tag{6}$$

for $i = 1, \ldots, m$, where $L = T - U$ and Q_i are the generalized forces in the out-of-plane direction, in this case the aerodynamic loads, given by

$$Q_j(t) = \int_S \Delta p(x, y, t) \frac{\partial w}{\partial r_j} \mathrm{d}S \tag{7}$$

where $\Delta p(x, y, t)$ is the pressure difference acting on point x, y at time t and S is the area of the wing.

For any set of mode shapes, it can be shown that Lagrange's equations can be written in matrix form as

$$\begin{aligned} \mathbf{A}_1\mathbf{p} + \mathbf{B}_1\mathbf{q} + \mathbf{C}_1(\mathbf{r} \otimes \mathbf{r}) &= \mathbf{0} \\ \mathbf{A}_2\mathbf{p} + \mathbf{B}_2\mathbf{q} + \mathbf{C}_2(\mathbf{r} \otimes \mathbf{r}) &= \mathbf{0} \\ \mathbf{A}\ddot{\mathbf{r}} + \mathbf{E}\mathbf{r} + \mathbf{N}_1(\mathbf{p} \otimes \mathbf{r}) + \mathbf{N}_2(\mathbf{q} \otimes \mathbf{r}) + \mathbf{N}_3(\mathbf{r} \otimes \mathbf{r} \otimes \mathbf{r}) &= \mathbf{Q}(t) \end{aligned} \tag{8}$$

where $\mathbf{A}_1$, $\mathbf{B}_1$ are $m_p \times m_p$ matrices, $\mathbf{C}_1$ is $m_p \times m_r^2$, $\mathbf{A}_2$, $\mathbf{B}_2$ are $m_q \times m_q$, $\mathbf{C}_2$ is $m_q \times m_r^2$, $\mathbf{A}$, $\mathbf{E}$ are $m_r \times m_r$, $\mathbf{N}_1$ is $m_r \times m_p m_r$, $\mathbf{N}_2$ is $m_r \times m_q m_r$ and $\mathbf{N}_3$ is $m_r \times m_r^3$. Furthermore, the symbol $\otimes$ denotes the Kroneker product of two vectors or matrices. The column vectors $\mathbf{p}$, $\mathbf{q}$ and $\mathbf{r}$ contain the p_j, q_j and r_j generalized coordinates respectively and the column vector $\mathbf{Q}$ contains the r generalized aerodynamics forces.

Equations 8 constitute a set of $m_p + m_q + m_r$ nonlinear differential equations to be solved for the generalized coordinate vectors $\mathbf{p}$, $\mathbf{q}$ and $\mathbf{r}$. The size of the problem can be reduced by solving the first two equations in terms of $\mathbf{r}$ and substituting back into the third equation [9], leading to

$$\mathbf{A}\ddot{\mathbf{r}} + \mathbf{E}\mathbf{r} + \mathbf{N}_1 \left[(\mathbf{R}_1(\mathbf{r} \otimes \mathbf{r})) \otimes \mathbf{r} \right] + \mathbf{N}_2 \left[(\mathbf{R}_2(\mathbf{r} \otimes \mathbf{r})) \otimes \mathbf{r} \right] + \mathbf{N}_3(\mathbf{r} \otimes \mathbf{r} \otimes \mathbf{r}) = \mathbf{Q}(t) \tag{9}$$

where

$$\begin{aligned}\mathbf{R}_1 &= -\left(\mathbf{A}_1^{-1}+\mathbf{A}_1^{-1}\mathbf{B}_1\left(\mathbf{B}_2-\mathbf{A}_2\mathbf{A}_1^{-1}\mathbf{B}_1\right)^{-1}\mathbf{A}_2\mathbf{A}_1^{-1}\right)\mathbf{C}_1 \\ &\quad +\mathbf{A}_1^{-1}\mathbf{B}_1\left(\mathbf{B}_2-\mathbf{A}_2\mathbf{A}_1^{-1}\mathbf{B}_1\right)^{-1}\mathbf{C}_2 \\ \mathbf{R}_2 &= \left(\mathbf{B}_2-\mathbf{A}_2\mathbf{A}_1^{-1}\mathbf{B}_1\right)^{-1}\mathbf{A}_2\mathbf{A}_1^{-1}\mathbf{C}_1-\left(\mathbf{B}_2-\mathbf{A}_2\mathbf{A}_1^{-1}\mathbf{B}_1\right)^{-1}\mathbf{C}_2 \end{aligned} \tag{10}$$

3.1 Aerodynamic modelling

The generalized aerodynamic forces in equation 9 are calculated by applying the unsteady Vortex Lattice Method [10]. Figure 3 demonstrates the discretization scheme for the wing and wake. Geometric panels are defined on the mean (camber) surface of the wing and vortex rings are placed on them, such that the leading edge of each vortex ring coincides with the quarter-chord line of each panel. The impermeability boundary condition is imposed on control points placed on the three-quarter-chord of each panel. Vortex rings are also placed in the wake behind the wing, the leading edge of the first wake ring coinciding with the trailing edge of the last bound vortex ring. Therefore, the wing is discretized into m chordwise and n spanwise panels and its wake is described by m_w chordwise and n spanwise vortex rings. The wing is immersed in a free stream with velocity $\mathbf{U}_\infty = [U\ V\ W]$, i.e. with airspeed $Q_\infty = |\mathbf{U}_\infty|$ and direction $\hat{\mathbf{u}} = [U\ V\ W]/Q_\infty$. The wake is flat and propagates in the streamwise direction with the free stream airspeed. The chordwise spacing of the wake vortex rings is chosen as c/m, where c is the chord.

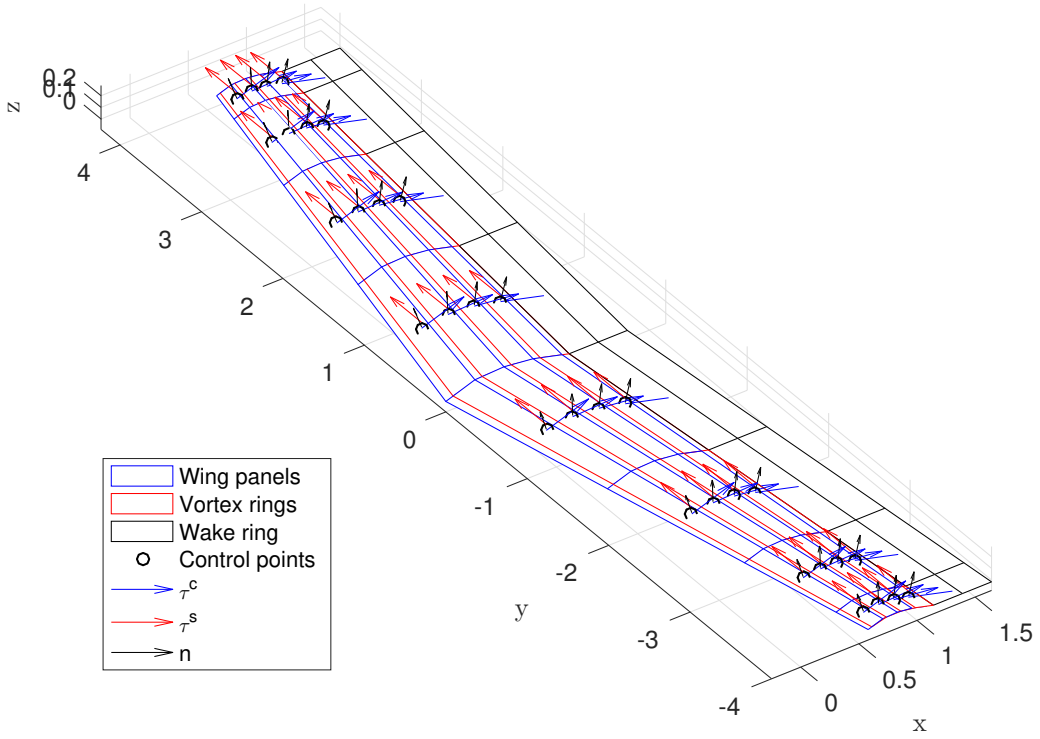

Figure 3: Wing discretization for the Vortex Lattice method

The geometries of the wing and wake remain unchanged (frozen) throughout the time history. Structural motion is represented only aerodynamically, by introducing a downwash term caused

by structural motion in the z direction (in-plane motion is ignored). The impermeability boundary condition is then formulated as

$$Q_\infty \text{diag}\left(\hat{\mathbf{U}}\mathbf{n}^T\right) - U\mathbf{w}_x\mathbf{r}(t) - \mathbf{w}\dot{\mathbf{r}}(t) + \mathbf{A}_b\boldsymbol{\Gamma}_b(t) + \mathbf{A}_w\boldsymbol{\Gamma}_w(t) = 0 \tag{11}$$

where $\hat{\mathbf{U}}$ is the $mn \times 3$ matrix whose rows are all equal to $\hat{\mathbf{u}}$, $\mathbf{n}$ is the $mn \times 3$ matrix of unit vectors normal to the surface of the panels (see figure 3), U is the x-component of the free stream velocity, $\mathbf{w}$ is a $mn \times 1$ vector of out-of-plane mode shapes (resampled versions of the w_j mode shapes of equation 1), $\mathbf{A}_b$ is the $mn \times mn$ influence coefficient matrix of the bound vorticity, $\boldsymbol{\Gamma}_b(t)$ is the $mn \times 1$ vector of the strengths of the bound vortex rings, $\mathbf{A}_w$ is the $m_w n \times m_w n$ influence coefficient matrix of the wake vorticity and $\boldsymbol{\Gamma}_w(t)$ is the $m_w n \times 1$ vector of the strengths of the wake vortex rings.

In order to satisfy the Kutta condition, the trailing bound vortex ring is shed into the wake at the next time instance, such that the leading row of wake vortices at time t has the strength of the trailing row of bound vortices at time $t - \Delta t$. Consequently, the wake vortex strength becomes

$$\boldsymbol{\Gamma}_w(t) = \begin{pmatrix} \mathbf{P}_c\boldsymbol{\Gamma}_b(t - \Delta t) \\ \mathbf{P}_c\boldsymbol{\Gamma}_b(t - 2\Delta t) \\ \vdots \\ \mathbf{P}_c\boldsymbol{\Gamma}_b(t - m_w\Delta t) \end{pmatrix}$$

where $\mathbf{P}_c$ is a $n \times mn$ matrix that is used to select only the trailing spanwise bound vortex segments. Note that Δt is the time it takes for a row of wake vortices to move by c/m with the free stream airspeed, so that $\Delta t = c/mU$. This description of $\boldsymbol{\Gamma}_w(t)$ is still not practical since it contains values of the bound voriticity from previous time steps. This problem can be resolved by taking the Fourier Transform of equation 11, such that

$$Q_\infty \text{diag}\left(\hat{\mathbf{U}}\mathbf{n}^T\right)\delta(\omega) - U\mathbf{w}_x\mathbf{r}(\omega) - i\omega\mathbf{w}\mathbf{r}(\omega) + \mathbf{A}_b\boldsymbol{\Gamma}_b(\omega) + \mathbf{A}_w\boldsymbol{\Gamma}_w(\omega) = 0 \tag{12}$$

where $\delta(\omega)$ is the Dirac delta function and ω is the frequency. The wake vorticity can now be written as

$$\boldsymbol{\Gamma}_w(\omega) = \mathbf{P}_e(\omega)\mathbf{P}_c\boldsymbol{\Gamma}_b(\omega) \tag{13}$$

where

$$\mathbf{P}_e(\omega) = \begin{pmatrix} \mathbf{I}_n e^{-i\omega\Delta t} \\ \mathbf{I}_n e^{-i\omega 2\Delta t} \\ \vdots \\ \mathbf{I}_n e^{-i\omega m_w\Delta t} \end{pmatrix}$$

Substituting equation 13 into equation 12 and solving for $\boldsymbol{\Gamma}_b(\omega)$ yields

$$\boldsymbol{\Gamma}_b(\omega) = -\left(\mathbf{A}_b + \mathbf{A}_w\mathbf{P}_e(\omega)\mathbf{P}_c\right)^{-1}\left(\text{diag}\left(Q_\infty\hat{\mathbf{U}}\mathbf{n}^T\right)\delta(\omega) - \left(U\mathbf{w}_x + i\omega\mathbf{w}\right)\mathbf{r}(\omega)\right) \tag{14}$$

The value of $\boldsymbol{\Gamma}_b(\omega)$ now depends exclusively on the constant geometry of the wing and wake, the free stream airspeed and the downwash induced by the modal deformations.

The aerodynamic normal force acting on the panels can be obtained from [10, 11]

$$\begin{aligned} \mathbf{L} \;=\; & \rho\left(\text{diag}\left((Q_\infty\hat{\mathbf{U}} + \mathbf{U}_w)\boldsymbol{\tau}_c^T\right) - \left(U\frac{\partial\mathbf{z}}{\partial x} + \frac{\partial\mathbf{z}}{\partial t}\right)\circ\boldsymbol{\tau}_{c_z}\right)\circ\mathbf{G}_c\boldsymbol{\Gamma}_b \\ & +\rho\left(\text{diag}\left((Q_\infty\hat{\mathbf{U}} + \mathbf{U}_w)\boldsymbol{\tau}_s^T\right) - \left(U\frac{\partial\mathbf{z}}{\partial x} + \frac{\partial\mathbf{z}}{\partial t}\right)\circ\boldsymbol{\tau}_{s_z}\right)\circ\mathbf{G}_s\boldsymbol{\Gamma}_b \\ & +\rho\mathbf{G}_A\dot{\boldsymbol{\Gamma}}_b \end{aligned} \tag{15}$$

where $\mathbf{U}_w$ is a $mn \times 3$ vector of flow speeds induced by the wake, $\boldsymbol{\tau}_c$ and $\boldsymbol{\tau}_s$ are $mn \times 3$ matrices containing the spanwise and chordwise tangential vectors, $\boldsymbol{\tau}_{c_z}$ and $\boldsymbol{\tau}_{s_z}$ are $mn \times 1$ vectors of the z-components only of the chordwise and spanwise tangent vectors and the $\circ$ symbol denotes the Hadamard product, i.e. element-by-element multiplication of vectors and/or matrices with identical dimensions. The matrices $\mathbf{G}_c$ and $\mathbf{G}_s$ are sparse matrices that, when post-multiplied by $\boldsymbol{\Gamma}_b$, form the products $(\Gamma_{i,j} - \Gamma_{i-1,j})A_{i,j}/\Delta c_{i,j}$ and $(\Gamma_{i,j} - \Gamma_{i,j-1})A_{i,j}/\Delta s_{i,j}$ for all panels in matrix form respectively. The area of panel i, j is denoted by $A_{i,j}$, its chord by $\Delta c_{i,j}$ and its span by $\Delta s_{i,j}$. Finally, $\mathbf{G}_A$ is a $mn \times mn$ diagonal matrix whose diagonal elements are $A_{i,j}$.

After linearisation, equation 15 becomes

$$\mathbf{L}(t) = \rho Q_\infty \left(\operatorname{diag}\left(\hat{\mathbf{U}}\boldsymbol{\tau}_c^T\right) \circ \mathbf{G}_c\boldsymbol{\Gamma}_b(t) + \operatorname{diag}\left(\hat{\mathbf{U}}\boldsymbol{\tau}_s^T\right) \circ \mathbf{G}_s\boldsymbol{\Gamma}_b(t) \right) + \rho \mathbf{G}_A \dot{\boldsymbol{\Gamma}}_b(t) \tag{16}$$

Taking the Fourier Transform of this equation results in

$$\mathbf{L}(\omega) = \rho \left(Q_\infty \mathbf{G}_{cs} + i\omega \mathbf{G}_A \right) \boldsymbol{\Gamma}_b(\omega) \tag{17}$$

where

$$\begin{aligned} \mathbf{G}_{cs} \;=\; & \left(\operatorname{diag}\left(\hat{\mathbf{U}}\boldsymbol{\tau}_c^T\right) \;\; \operatorname{diag}\left(\hat{\mathbf{U}}\boldsymbol{\tau}_c^T\right) \;\; \dots \;\; \operatorname{diag}\left(\hat{\mathbf{U}}\boldsymbol{\tau}_c^T\right) \right) \circ \mathbf{G}_c \\ & + \left(\operatorname{diag}\left(\hat{\mathbf{U}}\boldsymbol{\tau}_s^T\right) \;\; \operatorname{diag}\left(\hat{\mathbf{U}}\boldsymbol{\tau}_s^T\right) \;\; \dots \;\; \operatorname{diag}\left(\hat{\mathbf{U}}\boldsymbol{\tau}_s^T\right) \right) \circ \mathbf{G}_s \end{aligned}$$

Finally, after substituting from equation 14 and using the definition of the reduced frequency $k = \omega b/Q_\infty$, where b is the half-chord, the lift equation becomes

$$\mathbf{L}(k) = -\rho Q_\infty^2 \left(\mathbf{L}_0(k) - \mathbf{L}_1(k)\mathbf{r}(k) \right) \tag{18}$$

where

$$\mathbf{L}_0(k) = \left(\mathbf{G}_{cs} + i\frac{k}{b}\mathbf{G}_A \right) \left(\mathbf{A}_b + \mathbf{A}_w \mathbf{P}_e(k) \mathbf{P}_c \right)^{-1} \operatorname{diag}\left(\hat{\mathbf{U}}\mathbf{n}^T\right) \delta(k)$$

and

$$\mathbf{L}_1(k) = \left(\mathbf{G}_{cs} + i\frac{k}{b}\mathbf{G}_A \right) \left(\mathbf{A}_b + \mathbf{A}_w \mathbf{P}_e(k) \mathbf{P}_c \right)^{-1} \left(\mathbf{w}_x + i\frac{k}{b}\mathbf{w} \right)$$

where it was assumed that the angle of attack is small, such that $U \approx Q_\infty$. Furthermore, due to the presence of the Dirac delta function, $\mathbf{L}_0(k)$ can be written simply as

$$\mathbf{L}_0(k) = \mathbf{L}_0(0) = \mathbf{G}_{cs} \left(\mathbf{A}_b + \mathbf{A}_w \mathbf{P}_e(0) \mathbf{P}_c \right)^{-1} \operatorname{diag}\left(\hat{\mathbf{U}}\mathbf{n}^T\right) \delta(0)$$

Noting that $\Delta p \mathrm{d}S$ is an infinitesimal lift force and that the lift calculated by the VLM is not continuous but composed of discrete vectors on the control points of each panel the generalized forces can be written in matrix form as

$$\mathbf{Q}(k) = \left(\mathbf{L}(k)^T \mathbf{w}\mathbf{r} \right)^T \tag{19}$$

where $\mathbf{Q}(k)$ is the $n_m \times n_m$ generalized force matrix. Substituting from equation 18 the final form of the generalized force matrix is obtained

$$\mathbf{Q}(k) = -\rho Q_\infty^2 \left(\mathbf{Q}_0(0) - \mathbf{Q}_1(k)\mathbf{r}(k) \right) \tag{20}$$

where

$$\mathbf{Q}_0(0) = \left(\mathbf{L}_0(0)^T \mathbf{w} \right)^T \text{ and } \mathbf{Q}_1(k) = \left(\mathbf{L}_1(k)^T \mathbf{w} \right)^T$$

The generalized force of equation 20 is in the frequency domain and cannot be inserted into the time domain equations of motion 9. Roger's rational function approximation [12] is used in order to transform $\mathbf{Q}(k)$ into the time domain, such that

$$\mathbf{Q}(t) = -\rho Q_\infty^2 \mathbf{Q}_0 + \rho Q_\infty^2 \mathbf{S}_0 \mathbf{r}(t) + \rho Q_\infty b \mathbf{S}_1 \dot{\mathbf{r}}(t) + \rho b^2 \mathbf{S}_2 \ddot{\mathbf{r}}(t) + \rho Q_\infty^2 \sum_{i=1}^{n_l} \mathbf{S}_{2+i} \eta_i(t)$$

where $\mathbf{S}_0$ to $\mathbf{S}_{n_l}$ are aerodynamic stiffness, damping, mass and lag matrices, η_i are aerodynamic lags and n_l is the total number of lags retained in the approximation.

A complete set of time-domain aeroelastic equations can now be written by substituting into equations 9

$$\begin{aligned} \left(\mathbf{A} - \rho b^2 \mathbf{S}_2\right) \ddot{\mathbf{r}} + \left(-\rho Q_\infty b \mathbf{S}_1\right) \dot{\mathbf{r}} + \left(\mathbf{E} - \rho Q_\infty^2 \mathbf{S}_0\right) \mathbf{r} - \rho Q_\infty^2 \sum_{i=1}^{n_l} \mathbf{S}_{2+i} \eta_i & \\ + \mathbf{N}_1 \left[\left(\mathbf{R}_1(\mathbf{r} \otimes \mathbf{r})\right) \otimes \mathbf{r}\right] + \mathbf{N}_2 \left[\left(\mathbf{R}_2(\mathbf{r} \otimes \mathbf{r})\right) \otimes \mathbf{r}\right] + \mathbf{N}_3(\mathbf{r} \otimes \mathbf{r} \otimes \mathbf{r}) &= -\rho Q_\infty^2 \mathbf{Q}_0 \quad (21) \\ \dot{\eta}_i - \dot{\mathbf{r}} - \frac{U \gamma_i}{b} \eta_i &= \mathbf{0} \quad (22) \end{aligned}$$

where γ_i are the aerodynamic lag coefficients.

4 IMPLEMENTATION AND VALIDATION OF LINEAR MODEL

The generalised force matrix approach for the VLM detailed above is validated here using the flutter data from the wind tunnel experiments on flat plate wings with different sweep angles. Finite element models for the four AR=4 wings were constructed using MSC.Nastran, assuming that the plates were cantilevered. Modal mass and stiffness matrices and mode shapes were extracted from each model. For $\Lambda \neq 0$ all modes combine both bending and torsion but mode 1 is mostly first bending and more 3 is mostly first torsion. Figure 4 plots the first four mode shapes for the wing with $\Lambda = 10°$. It can be seen that mode 1 is indeed mostly bending, mode three mostly torsion, while the other two modes combine bending and torsion. The natural frequencies of the first five modes of vibration are tabulated in table 2 for all four wings. The table shows that the first torsion mode is not affected by the sweep but all the other modes are, albeit to different extents.

Mode	sweep $\Lambda = 0°$	sweep $\Lambda = 10°$	sweep $\Lambda = 20°$	sweep $\Lambda = 45°$
1	1.28 Hz	1.25 Hz	1.15 Hz	0.68 Hz
2	8.01 Hz	7.76 Hz	7.09 Hz	4.18 Hz
3	10.17 Hz	10.21 Hz	10.28 Hz	10.13 Hz
4	22.48 Hz	21.77 Hz	19.83 Hz	11.63 Hz
5	31.42 Hz	31.49 Hz	31.55 Hz	22.69 Hz

Table 2: Finite element modal frequencies for AR=4 wings

The mode shapes obtained from the finite element models were interpolated linearly on the control points of the VLM panels. However, as the flat plates are cantilevered on one end, a representative aerodynamic model can only be obtained if the wing is mirrored around its centreline so that a symmetric flowfield can be set up. Hence, the wings modelled with the VLM spanned from -0.8 m to $+0.8$ m and were perfectly symmetrical.

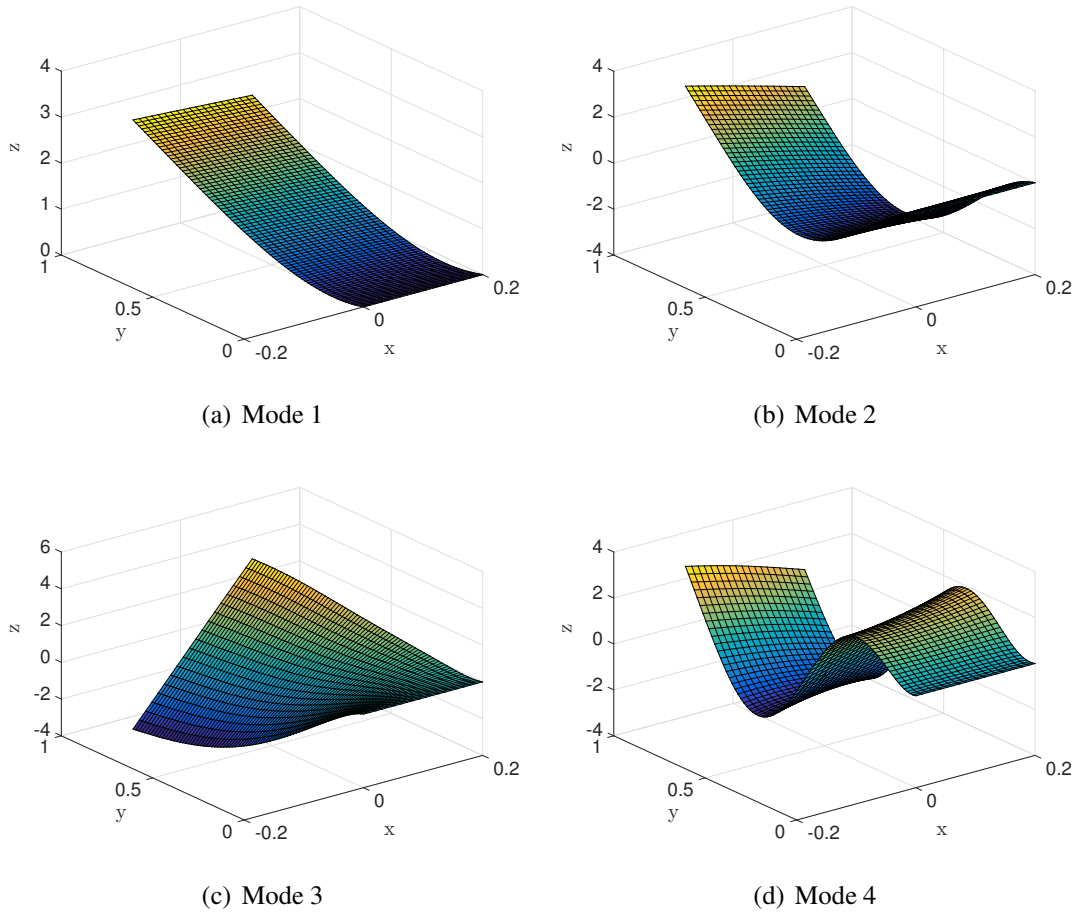

(a) Mode 1

(b) Mode 2

(c) Mode 3

(d) Mode 4

Figure 4: Finite element mode shapes for the wing with AR=4, $\Lambda = 10°$

Figure 5 plots the flutter speed and frequency predictions obtained from the VLM aeroelastic model for all wings and compares them to the experimental measurements. It can be seen that the predicted flutter speed follows the trend of the experimental data but is systematically lower by about 0.9 m/s, except for the unswept wing. The flutter frequency behaves in a similar way, following the trend of the experimental data but being systematically lower by about 0.8 Hz. Furthermore, for the unswept wing, the flutter frequency is significantly lower than the experimental observation.

5 NONLINEAR RESULTS

The linear model only requires out-of-plane modes w_j. For the nonlinear model, the in-plane modes u_j and v_j must also be defined. Attar [5] showed that a good strategy is to use the same out-of-plane modes for the in-plane modes, such that $u_j = v_j = w_j$ and $m_p = m_q = m_r$. The same strategy was used in the same work for different values of m_r.

The complete nonlinear equations of motion 21 and 22 were solved using a numerical continuation scheme based on finite difference discretization [9]. The solution procedure started at the linear flutter airspeed, where the limit cycle oscillations have zero amplitude and frequency equal to the flutter frequency. The next step was to integrate numerically equations 21 and 22 at a slightly higher airspeed $Q_F + \Delta Q$ until the response settled onto a limit cycle, where Q_F is the flutter speed and ΔQ is a small airspeed increment. These first two solutions were used to predict the limit cycle at airspeed $Q_F + 2\Delta Q$. This prediction was corrected by applying

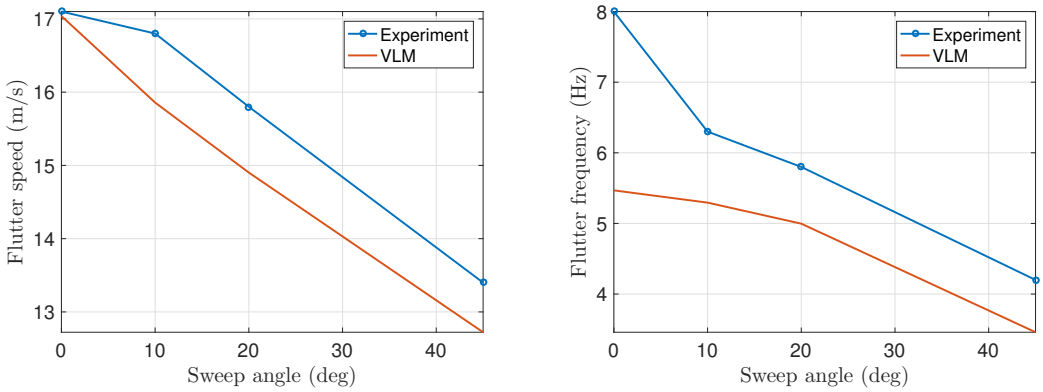

(a) Flutter speed (b) Flutter Frequency

Figure 5: Flutter airspeed and frequency predictions for all AR=4 wings

a Newton-Raphson procedure. Subsequently, a pseudo-arclength continuation scheme was applied in order to allow for folds and other bifurcations in the limit cycle branch.

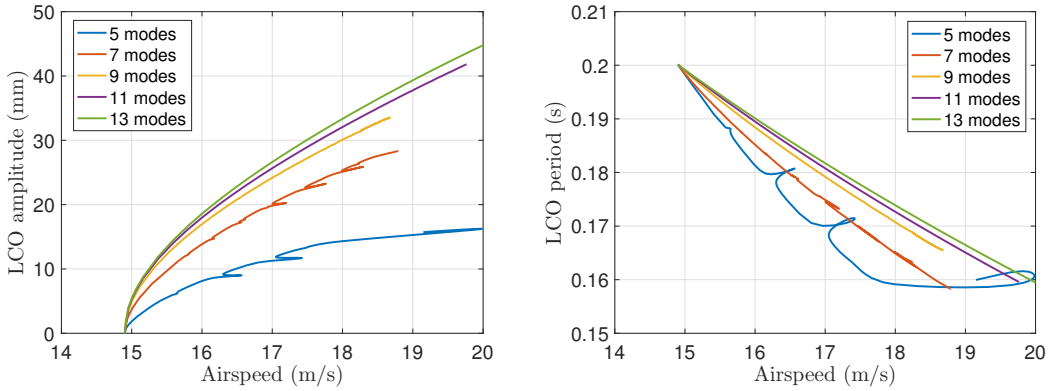

(a) Amplitude (b) Period

Figure 6: Limit cycle amplitude and period variation with airspeed for AR=4, $\Lambda 20^\circ$ wing

Figure 6 plots the predicted limit cycle amplitude and period variation with airspeed for the AR=4, $\Lambda 20^\circ$ wing, for increasing number of modes. The amplitude plotted is that of the out-of-plane displacement of the wingtip's trailing edge. It is clear that the solution converges as the number of modes increases. For $m_r = 5$ and $m_r = 7$, the limit cycle branch has low amplitude and features several folds. For $m_r = 13$ the solution is nearly converged, the limit cycle amplitude at 19 m/s is nearly 40 mm and there are no folds in the branch inside the airspeed range of interest.

Figure 6 compares the limit cycle amplitude and frequency simulation predictions to the experimental measurement. It can be seen that the frequency variation with airspeed is predicted quite accurately. The simulated amplitude is of the right order of magnitude but its variation with airspeed is different to the one measured during the experiments. The slope of the amplitude decreases with airspeed for the simulated results while it increases for the experimental measurements. This difference may be due to the fact that, as the amplitude increases, additional physics can come into play, such as viscous effects and stall flutter. The linear aerodynamic model used in the present work cannot represent such phenomena.

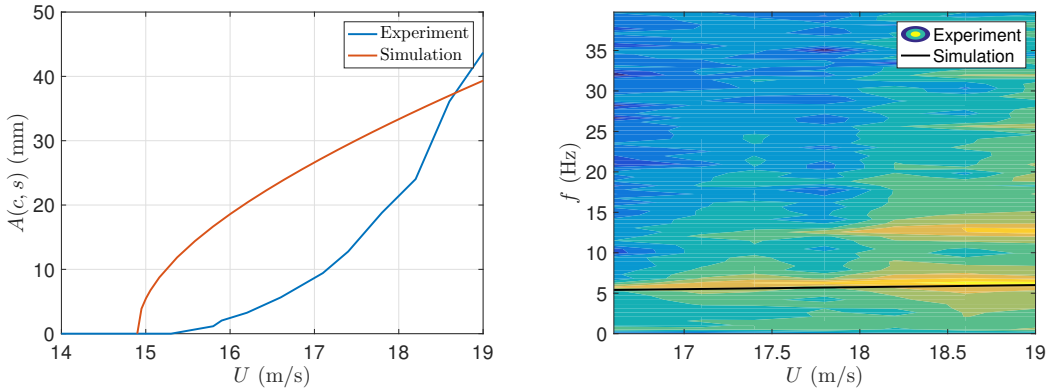

(a) Amplitude (b) Period

Figure 7: Comparison of experimental and simulated limit cycle amplitude and frequency for AR=4, $\Lambda 20°$ wing

6 CONCLUSIONS

This work presents a closed form state-space model of the nonlinear aeroelastic response of thin cantilevered flat plates in low speed airflows. The model is based on a combination of Von Kármán thin plate theory and a linearized continuous time vortex lattice aerodynamic model. Comparison to experimental measurements in a low speed wind tunnel shows that the model predicts the linear flutter airspeed and frequency with reasonable accuracy. It also predicts limit cycles in the correct airspeed range and with accurate frequency. The predicted limit cycle amplitude has the right order of magnitude but its variation with airspeed is different to the one observed experimentally. This difference may be due to additional physics that is not represented by the model, such as viscous effects and stall flutter.

7 REFERENCES

[1] Weiliang, Y. and Dowell, E. H. (1991). Limit cycle oscillation of a fluttering cantilever plate. *AIAA Journal*, 29(11), 1929–1936.

[2] Tang, D., Dowell, E. H., and Hall, K. C. (1999). Limit cycle oscillations of a cantilevered wing in low subsonic flow. *AIAA Journal*, 37(3), 364–371.

[3] Tang, D., Henry, J. K., and Dowell, E. H. (1999). Limit cycle oscillations of delta wing models in low subsonic flow. *AIAA Journal*, 37(11), 1355–1362.

[4] Attar, P. and Gordnier, R. (2001). Aeroelastic prediction of the limit cycle oscillations of a cropped delta wing. *Journal of Fluids and Structures*, 22(1), 45–58.

[5] Attar, P. J. (2007). Cantilevered plate Rayleigh-Ritz trial function selection for von Kármán's plate equations. *Journal of Aircraft*, 44(2), 654–661.

[6] Attar, P., Dowell, E., and Tang, D. (2003). A theoretical and experimental investigation of the effects of a steady angle of attack on the nonlinear flutter of a delta wing plate model. *Journal of Fluids and Structures*, 17(2), 243–259.

[7] Tang, D. and Dowell, E. H. (2001). Effects of angle of attack on nonlinear flutter of a delta wing. *AIAA Journal*, 39(1), 15–21.

[8] Korbahti, B., Kagambage, E., Andrianne, T., et al. (2011). Subcritical, nontypical and period-doubling bifurcations of a delta wing in a low speed wind tunnel. *Journal of Fluids and Structures*, 27(3), 408–426.

[9] Dimitriadis, G. (2017). *Introduction to nonlinear aeroelasticity*. Chichester, West Sussex, UK: John Wiley & Sons, Inc.

[10] Katz, J. and Plotkin, A. (2001). *Low Speed Aerodynamics*. Cambridge University Press.

[11] Simpson, R. J. S., Palacios, R., and Murua, J. (2013). Induced-drag calculations in the unsteady vortex lattice method. *AIAA Journal*, 51(7), 1775–1779.

[12] Roger, K. L. (1977). Airplane math modelling methods for active control design. Report AGARD-CP-228, AGARD.

COPYRIGHT STATEMENT